International Journal of Heat and Mass Transfer 52 (2009) 3024–3031

Contents lists available at ScienceDirect

International Journal of Heat and Mass Transfer

journal homepage: www.elsevier.com/locate/ijhmt

Spatial and temporal coherence of thermal radiation in asymmetric Fabry–Perot resonance cavities

L.P. Wang [a], B.J. Lee [b], X.J. Wang [a], Z.M. Zhang [a,*]

[a] George W. Woodruff School of Mechanical Engineering, Georgia Institute of Technology, Atlanta, GA 30332, USA
[b] Department of Mechanical Engineering and Materials Science, University of Pittsburgh, Pittsburgh, PA 15261, USA

ARTICLE INFO

Article history:
Received 28 May 2008
Accepted 23 January 2009
Available online 1 April 2009

Keywords:
Coherent thermal emission
Fabry–Perot
Optical resonance
Thin film

ABSTRACT

There has been an increased interest on the development of micro/nanostructures with desired radiative properties for energy conversion systems and radiative cooling devices. A detailed experimental study is reported on the spatial and temporal coherence of thermal radiation in asymmetric Fabry–Perot resonance cavities. The reflectance of the fabricated samples was measured for both polarizations using a Fourier-transform infrared spectrometer, at several incident angles in the near-infrared region, and a laser scatterometer at the wavelength of 891 nm. The spectral measurement demonstrates sharp reflectance dips, while narrow angular lobes are observed in the angle-resolved measurement. Experimental results suggest strong spectral and directional selectivity in thermal emission, which is related to the reflection by Kirchhoff's law since the samples are opaque. Theoretical calculations with the fitting geometric parameters agree well with the measurement results. This easy-to-fabricate structure has potential applications in solar cells, thermophotovoltaic devices, and radiation emitters.

1. Introduction

Thermal sources are commonly considered to be incoherent in the sense that the emissivity exhibits broad spectral and quasi-isotropic angular distributions, since the thermally excited charged particles generate randomly oriented dipoles in the medium. However, much attention has been drawn on tailoring thermal emission after the observation of directional emission in doped-Si gratings that support the organ-pipe modes [1]. The spectral and directional selectivity of thermal emission can be used for radiation filters, absorbers, and emitters, which are essential for applications such as solar cells, thermophotovoltaic systems, radiation detectors, and radiative cooling devices [2].

Recently, there has been increased interest in developing micro/nanostructures to achieve coherent thermal emission. Laroche et al. [3] reported that surface relief grating constructed with tungsten could generate highly directional emission (spatial coherence) in the near infrared. The basic mechanism is that gratings enable the coupling between surface plasmons and propagation waves. Two-dimensional tungsten gratings were also shown to exhibit spectral selectivity (temporal coherence) for thermal radiation [4], and the confined modes in the microcavities were responsible for the strong emission peaks. A recent study also showed that the excitation of magnetic polaritons between periodic gratings and a metallic film enabled coherent emission for transverse magnetic (TM) waves [5]. Furthermore, surface waves have been demonstrated in multilayer structures, such as one-dimensional (1D) photonic crystals (PC) with an attenuated total reflection configuration [6,7] and a metallic thin film deposited on a semi-infinite 1D PC [8]. Researchers also suggested spectral and directional selectivity in thermal radiation of a PC-on-SiC structure for both polarizations [9,10]. The spatial and temporal coherence of a truncated PC atop a Ag film was experimentally investigated for both polarizations in the near-infrared (IR) region, and the existence of surface wave at the interface was validated by observation with reflectance spectroscopy [11,12].

Besides excitation of surface plasmons and/or magnetic polaritons, interference effects in planar structures can also be utilized to achieve coherent emission, such as in a resonance cavity with highly reflective coatings [13–15]. The reflector can be made of a metallic layer, doped Si, or Bragg mirrors. Fabry–Perot resonators have been applied to build transmission filters and high-resolution spectrometry [16,17]. More recently, it has been shown that an asymmetric Fabry–Perot resonator made of a SiO_2 cavity, sandwiched between coated a thin Ag film and an opaque Ag film, exhibits spectral selectivity with deep reflectance valleys at near normal incidence, suggesting that sharp emissivity peaks can be achieved. Further research is needed on the angular and polarization dependence of these structures.

This paper describes a detailed experimental study on the spatial and temporal coherence of thermal emission from asymmetric

* Corresponding author. Tel.: +1 404 385 4225; fax: +1 404 894 8496.
E-mail address: zhuomin.zhang@me.gatech.edu (Z.M. Zhang).

0017-9310/$ - see front matter © 2009 Elsevier Ltd. All rights reserved.
doi:10.1016/j.ijheatmasstransfer.2009.01.042

Nomenclature

d	film thickness (m)
i	$\sqrt{-1}$
n	refractive index
R	reflectance
r	reflection coefficient
T	transmittance
t	transmission coefficient

Greek symbols

α	absorptance
β	phase shift in the thin film (rad)
$\varepsilon_{\lambda,\theta}$	spectral–directional emissivity
ζ	$\lvert t_a t_b - r_a r_b \rvert$
θ	polar angle (°)
θ_0	polar angle at the resonance (°)
λ	wavelength in vacuum (μm)
ν	wavenumber (cm^{-1})
$\Delta\nu$	free spectral range (cm^{-1})
$\delta\nu$	full width at half maximum (or minimum) (cm^{-1})
ρ	magnitude of the reflection coefficient, $\rho = \lvert r \rvert$
τ	magnitude square of the transmission coefficient, $\tau = \lvert t \rvert^2$
φ	phase angle of the reflection coefficient (rad)
ψ	phase shift (rad)

Subscripts

a	incidence from air to SiO_2 through the thin Au film
b	incidence from SiO_2 to air through the thin Au film
c	dielectric cavity (SiO_2 film)
f	Au film
i	incidence
s	bottom Au layer

Fabry–Perot resonators. The structures are composed of a SiO_2 optical cavity with a thin Au film (less than 30 nm) and a 200-nm Au film deposited on a Si substrate. Three samples with different metal and dielectric film thicknesses were fabricated. The spectral reflectance was measured with a Fourier-transform infrared (FTIR) spectrometer at incidence angles of 10°, 30°, and 45°, respectively, for both transverse electric (TE) and TM waves. Angle-resolved reflectance measurements were performed with a custom-designed three-axis automated scatterometer (TAAS) at the wavelength of 891 nm using a diode laser source. The measurement results clearly show the spectral and directional selectivity in thermal emission of the fabricated samples, which can be well explained by theoretical calculations using the fitting geometric parameters and the published optical constants of the metal and dielectric materials.

2. Radiative properties of the asymmetric Fabry–Perot resonator

The proposed Fabry–Perot resonance cavity is schematically shown in Fig. 1. It is different from the conventional Fabry–Perot resonator made of two parallel reflectors separated at a finite distance, because the bottom metal layer can be treated as semi-infinite and is opaque to incident radiation. In other words, the geometry of proposed structure is asymmetric with respect to the dielectric cavity. In general, high reflection from the boundaries of the resonance cavity is essential for the sharp spectral peak at the resonance condition [17]. In the present study, we employed SiO_2 to form the optical cavity and Au as the reflective coating on both sides of the dielectric cavity. Fig. 1 also illustrates the reflection and transmission coefficients at the boundaries of the Fabry–Perot resonator. It should be noted that t_a and r_a are, respectively, the transmission and reflection coefficients from air to SiO_2, and t_b and r_b are, respectively, the transmission and reflection coefficients from SiO_2 to air, assuming that SiO_2 is semi-infinite. These coefficients depend on the complex refractive index and the thickness of Au, according to Airy's formulae. Furthermore, t_s and r_s are the Fresnel transmission and reflection coefficients at the interface between SiO_2 and Au. All the transmission and reflection coefficients are polarization dependent and the expressions can be found from Refs. [2,18] for either TE wave or TM wave. According to Airy's formulae, the reflection and transmission coefficients of the Fabry–Perot resonator can be expressed after superposition as follows [17]

$$r = r_a + \frac{t_a t_b r_s e^{i2\beta}}{1 - r_b r_s e^{i2\beta}} \tag{1}$$

and

$$t = \frac{t_a t_s e^{i\beta}}{1 - r_b r_s e^{i2\beta}} \tag{2}$$

where $\beta = 2\pi n_c d_c \cos\theta_c / \lambda$ is the phase shift upon traveling inside the cavity with the refractive index n_c and the thickness d_c. As shown in Fig. 1, θ_c is the refraction angle in the dielectric cavity. The spectral–directional reflectance and transmittance of the Fabry–Perot cavity can be calculated from the reflection and transmission coefficients as

$$R = rr^* \tag{3}$$

and

$$T = \frac{\mathrm{Re}(\cos\theta_s / n_s)}{\mathrm{Re}(\cos\theta_i / n_i)} tt^* \text{ for TM waves} \tag{4a}$$

or

$$T = \frac{\mathrm{Re}(n_s \cos\theta_s)}{\mathrm{Re}(n_i \cos\theta_i)} tt^* \text{ for TE waves} \tag{4b}$$

where Re() indicates the real part of a complex quantity, the asterisk denotes the complex conjugate, and n_i and n_s are the complex refractive indices of air and Au, respectively. The square of the reflection and transmission coefficients can be simplified using Eqs. (1) and (2) as follows:

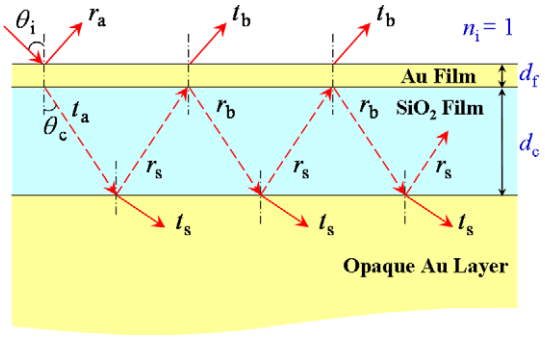

Fig. 1. Schematic of the asymmetric Fabry–Perot resonance cavity, with illustration of the reflection and transmission coefficients at the boundaries.

$$rr^* = \frac{(\rho_a + \rho_s\zeta)^2 - 4\rho_a\rho_s\zeta\sin^2\psi_1}{(1-\rho_b\rho_s)^2 + 4\rho_b\rho_s\sin^2\psi_2} \quad (5)$$

and

$$tt^* = \frac{\tau_a\tau_s}{(1-\rho_b\rho_s)^2 + 4\rho_b\rho_s\sin^2\psi_2} \quad (6)$$

where $\rho = |r_j|$ and $\tau = t_j t_j^*$ with j representing a, b, or s as the corresponding subscript, $\zeta = |t_a t_b - r_a r_b|$, $\psi_1 = (2\beta - \varphi_a + \varphi_s + \varphi_\zeta)/2$, and $\psi_2 = (2\beta + \varphi_b + \varphi_s)/2$, with $\varphi_j = \arg(r_j)$ and $\varphi_\zeta = \arg(t_a t_b - r_a r_b)$. In the proposed structure, the thickness of bottom Au layer is set to be much greater than the radiation penetration depth (i.e., photon mean free path); thus the bottom Au layer can be assumed semi-infinite. Note that T represents the fraction of energy transmitted into the Au layer and will eventually be absorbed. Since the bottom Au layer is opaque, the spectral-directional emissivity of the Fabry–Perot cavity can be obtained as $\varepsilon_{\lambda,\theta} = 1 - R$ according to Kirchhoff's law [2], where R is calculated from Eq. (5). However, the thickness of the top Au film should be on the order of the radiation penetration depth to enable resonance inside the cavity.

3. Sample fabrication and measurements

3.1. Sample fabrication

To experimentally demonstrate that the proposed structure can be used as a coherent emission source, several samples were fabricated on Si substrates and their spectral and directional radiative properties were measured. The Si wafers are of 100 mm in diameter and 500 μm in thickness. A thin Ti film and a 200-nm Au film were subsequently deposited on the polished side of the Si substrate, after proper surface cleaning, using an e-beam evaporator without breaking its vacuum environment. A quartz crystal microbalance monitored the deposition thickness. The thin Ti film (about 20 nm) serves as an adhesive layer to prevent the Au film from peeling off. As long as the thickness is much greater than the penetration depth, this Au film can be treated as an opaque layer or a semi-infinite medium. Thus, the exact thicknesses of these bottom layers are not important. After the sample was cooled down in the e-beam evaporator, it was taken out and placed into a plasma-enhanced chemical vapor deposition (PECVD) chamber. SiO_2 thin film was deposited at 250 °C on the sample and on a bare Si piece as well. The thickness of the dielectric layer was measured from the reference Si piece using a reflectometer (Nanospec Film Analyzer 3000). The measurements indicate that the SiO_2 layer has less than 5% variation in thickness relative to the designed value. Afterwards, the sample was placed back into the e-beam evaporator and coated with a thin Au film (less than 30 nm). Because the quartz crystal monitor could not precisely determine the deposited thickness for very thin Au films, several trial-and-error tests were made in order to find the appropriate Au thickness for the Fabry–Perot resonance cavities. Because the resonance frequency and the minimum reflectance value are very sensitive to the thicknesses of the SiO_2 cavity and top Au film, the exact thicknesses of dielectric layer and Au film are determined later by fitting the reflectance measured by the FTIR spectrometer. Three samples (1, 2, and 3) with different SiO_2 cavity thicknesses and Au film thickness were fabricated to study the thicknesses effect. The samples were diced into 25 mm × 25 mm square pieces for measurements of the radiative properties.

3.2. Spectral radiative property measurement

An FTIR spectrometer was used to measure the spectral reflectance of the samples at near normal incidence (10°), as well as incidence angles of 30° and 45° using suitable specular reflectance accessories. The near-IR source, a quartz–halogen lamp with a tungsten filament, was used with a pyroelectric detector, which has an excellent linearity up to 13,000 cm^{-1} in wavenumber. At 10° incidence, the difference between TE and TM waves is negligibly small and the beam from the FTIR source is assumed to be unpolarized (i.e., average of the two polarizations). A wire-grid IR polarizer was used to measure the reflectance for TE and TM waves at 30° and 45° angles of incidence. In the measurements, the polarizer was intentionally tilted to eliminate multiple reflections [19]. Before the measurement, the near-IR source was turned on for more than 1 h, and the background signal was examined to be stable with less than 1% of fluctuation. The wavenumber range of the reflectance spectra was taken from 3000 to 13,000 cm^{-1}, with a resolution of 4 cm^{-1}. A sample holder with an aperture of 9 mm diameter limited the beam size on the sample. A mirror was fabricated by evaporating 200-nm Au film on a Si substrate and used as the reference. The background signal was measured without placing any sample (open aperture), and the signal was less than 0.5% of that with the mirror. The measurement of each sample was repeated eight times for both the sample spectrum and the reference spectrum. Each spectrum was actually the average of 64 scans. The spectral reflectance of the fabricated Fabry–Perot resonance cavities can be obtained by correcting the average over eight measurements with the mirror reflectance, which was calculated using the optical constants of gold from Ref. [20] for the corresponding incidence angle and polarization. The overall uncertainty of the measured reflectance was estimated to be 0.02, considering various possible sources of error, such as beam divergence, misalignment of sample, mirror reflectance, background signal, and repeatability.

3.3. Angle-resolved reflectance measurement

To experimentally study the directional radiative properties of the constructed Fabry–Perot resonance cavities, the laser scatterometer (TAAS) [21,22] was used to measure the specular reflectance of Sample 1 at different incidence angles for each polarization. TAAS has three movable stages to change the incidence and observation directions, which can be automatically controlled by a computer under the LabVIEW environment. A thermoelectric-cooled diode laser system was employed using a laser diode at the wavelength of 891 nm with a full width at half maximum (FWHM) bandwidth of 3 nm. A lock-in amplifier connected with a diode laser controller modulates the output power at 400 Hz. The output laser power is approximately 1 mW with a stability of a few tenths of a percent. The laser beam passed through a small iris and was collimated through a pair of lenses before going through a near-IR polarizer. A beamsplitter divided the ray into two beams: a transmitted beam that was in the same direction as the incidence and a reflected beam that was in the horizontal plane but perpendicular to the incidence. The transmitted beam was incident on the sample and the signal reflected by the sample was received by a movable Si detector. The reflected beam from the beamsplitter was sent to a stationary reference Si detector. The majority of the laser power is transmitted with a transmittance of about 85% for the TE wave and 95% for the TM wave. The synchronous voltage signals from the two detectors were collected by the lock-in amplifier through a trans-impedance preamplifier. The effect of background radiation (i.e., stray light) can be eliminated by only picking up the phase-locked signals at 400 Hz. In the present study, the specular reflectance of Sample 1 was measured at the incidence angles from 2° to 75° with 1° increment, except that in the range between 32° and 50°, where the increment was set at 0.2° in order to resolve the reflectance valley (emissivity peak). The uncertainty of the angle-resolved reflectance measurement was estimated to be 0.02 by calibration using a bare

Si sample and by evaluation of the standard deviation of repeated measurements.

4. Results and discussion

The measured reflectance spectra of the three samples at near normal incidence ($\theta_i = 10°$) are shown in Fig. 2. At this incidence angle, polarization effect is negligible. In the frequency range from 3000 to 13,000 cm^{-1} (the frequency unit is expressed in terms of wavenumber in the present study), there are two sharp reflectance dips arising from resonances in the dielectric cavity. It should be noted that due to the low signal-to-noise ratio at high frequencies, the spectra beyond 11,000 cm^{-1} exhibit large fluctuations. To further reduce the measurement noise, the reflectance at frequencies above the second valley was averaged over 21 consecutive data points (i.e., 10 points on the left and 10 points on the right) with respect to their central frequency. The plots shown in Fig. 2 are the spectra after the noise reduction. In order to determine the dielectric and Au film thicknesses of each sample, Eq. (5) was used to calculate the spectral reflectance at $\theta_i = 10°$ with d_c and d_f as the adjustable parameters. In the calculation, the optical constants of Au and SiO_2 were taken from Palik [20]. The initial values were obtained from the measured film thicknesses. The location of the resonance frequency is more sensitive to the SiO_2 thickness, while the magnitude of the reflectance minimum is more sensitive to the Au film thickness. The best fitting results can be obtained by iteratively modifying d_c and d_f and comparing the calculated spectra with that measured. The fitting parameters are tabulated in Table 1 for each sample, along with the free spectral range and the quality factor of the resonance as discussed in the following.

The free spectral range $\Delta\nu$ is the frequency interval between the two consecutive resonance dips. It can be seen that Samples 2 and 3 have similar SiO_2 thickness and free spectral range. For a dielectric film inside air, the free spectral range is determined by resonances inside the film and can be calculated from $\Delta\nu = 1/(2n_c d_c \cos\theta_c)$, assuming the refractive index of the dielectric is frequency independent [2]. Taking the average refractive index of SiO_2 as 1.44, the above equation gives for Sample 1 $\Delta\nu = 5623\ cm^{-1}$, which is more than 10% greater than the actual $\Delta\nu$ of 5050 cm^{-1}. This is caused by the phase shift upon reflection at the SiO_2 cavity boundaries. From Eqs. (5) and (6), the modulation of the transmittance and reflectance is determined by the modified phase angles ψ_1 and ψ_2. The maxima of T occur when the denominator of Eq. (6) is at its minima, that is,

$$2\psi_2 = 2\beta + \phi_b + \phi_s = 2m\pi \tag{7}$$

where m is an integer. Eq. (7) states that the resonance occurs if the total phase shift in the cavity is multiples of 2π, where standing waves exist in the cavity. As mentioned earlier, the absorptance of the bottom Au layer is $\alpha_s = T$ because it is opaque. The multiple reflections result in strong absorption in the top Au film as well, though at a nearby frequency. The absorptance of the top Au film

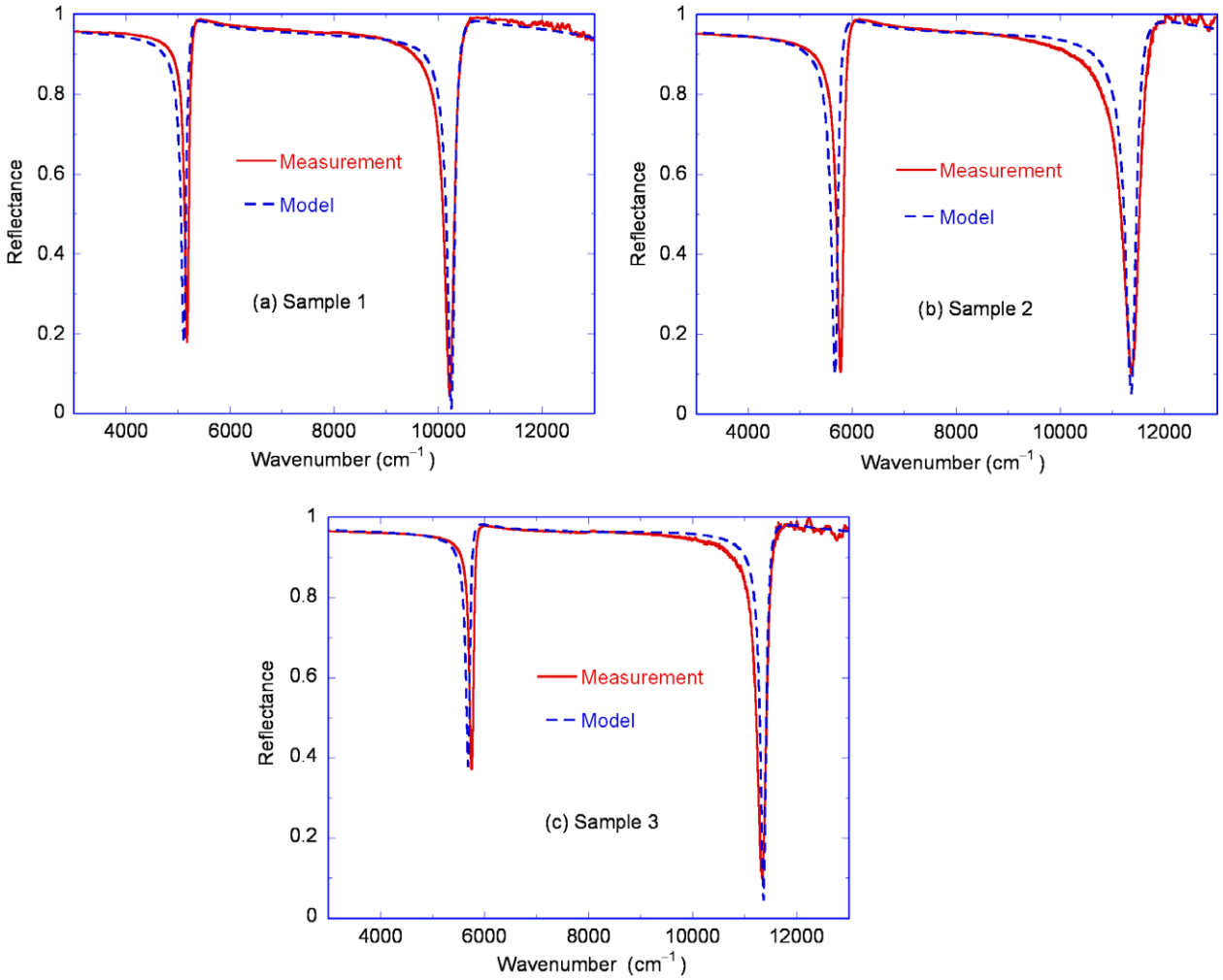

Fig. 2. Spectral reflectance of the fabricated Fabry–Perot resonators in the near-IR spectral region at $\theta_i = 10°$: (a) Sample 1; (b) Sample 2; (c) Sample 3.

Table 1
The measured free spectral range and quality factors, along with the fitted SiO_2 and Au film thicknesses based on the measurement results at an angle of incidence of 10°.

Sample No.	Free spectral range $\Delta\nu$ (cm^{-1})	SiO_2 thickness d_c (nm)	Au film thickness d_f (nm)	Quality factor Q at the 1st resonance	Quality factor Q at the 2nd resonance
1	5050	622	21	49.5	21.7
2	5576	553	20	34.4	13.9
3	5587	559	30	53.2	25.3

is $\alpha_f = 1 - R - T$ because the SiO_2 layer is nonabsorbing in the spectral range of interest. The absorptances of the top Au film and bottom Au layer are shown in Fig. 3, which was calculated based on the fitting parameters for Sample 1. Interestingly, the absorptance α of the Fabry–Perot structure has a minimum on the right of the maximum, this explains why the reflectance R exhibits a maximum on the right of the minimum and the reflectance dip is asymmetric, as can be seen from Fig. 2. One can see from Eq. (3) that the reflectance minimum is determined by its numerator at the frequency that satisfies $\psi_1 = (m + 1/2)\pi$. It can be shown that the phase difference between ψ_1 and ψ_2 is close to $\pi/2$. Hence, the reflectance minimum occurs near the resonance condition given in Eq. (7). It should be noted that while there exist minima in T at frequencies where $\psi_2 = (m + 1/2)\pi$, it does not significantly affect α (or R) as can be seen from Fig. 3. As a matter of fact, away from the resonance condition, very little of the incident energy can reach the bottom Au layer; subsequently, the reflectance of the Fabry–Perot resonator is essentially the same as the reflectance when the SiO_2 layer is semi-infinite; that is, $R \approx R_a = r_a r_a^*$.

The existence of reflectance dips suggests that the Fabry–Perot resonators can be used to construct coherent emission sources, since $\varepsilon_{\lambda,\theta} = \alpha = 1 - R$. A measure of the sharpness of the emissivity peak, or the reflectance dip, is the quality factor defined as $Q = \Delta\nu/\delta\nu$ for Fabry–Perot resonance cavities, where $\delta\nu$ is the full width at half maximum, or minimum [17]. The Q factors for 10° angle of incidence at the two resonance frequencies are tabulated in Table 1 for each sample. Generally speaking, the peak width tends to broaden towards higher frequencies. This is why the quality factor at the second resonance frequency is about half of that at the first resonance frequency. Because Sample 2 has a thinner SiO_2 layer, the resonance frequencies increase, resulting in a lower Q factor for Sample 2. Samples 2 and 3 have similar SiO_2 thickness but Sample 3 has a thicker Au film. It can be seen that the Q factor is enhanced with increasing Au film thickness. However, the peak emissivity for Sample 3 at the first resonance frequency is not as high as can be seen from Fig. 2.

The effect of Au film thickness on the peak emissivity is further investigated near the resonance frequencies. The absorptances at the resonance wavenumbers around 5500 and 11,000 cm^{-1} are calculated for different film thickness d_f for given $d_c = 560$ nm at $\theta_i = 10°$. Note that the exact resonance frequency will vary somewhat with d_f. As shown in Fig. 4, there exist thickness values where the absorptance peak is maximized. However, the maxima of α_f, α_s, and α do not occur at the same d_f. It is interesting to see that more energy is absorbed by the thin Au film than by the bottom Au layer. For the first resonance, the spectral–directional emissivity is close to unity when $d_f = 12.5$ nm. In this case, about 80% of the energy is absorbed by the Au film. For the second resonance near 11,000 cm^{-1}, a

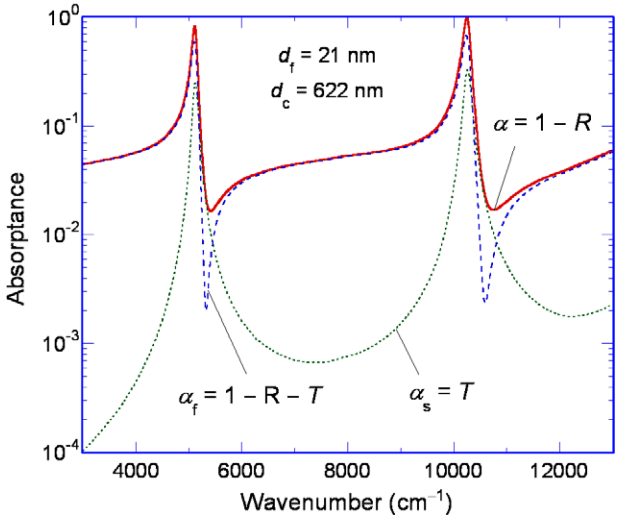

Fig. 3. Absorptance spectra calculated based on the geometric parameters for Sample 1 ($d_c = 622$ nm and $d_f = 21$ nm) for unpolarized waves at $\theta_i = 10°$.

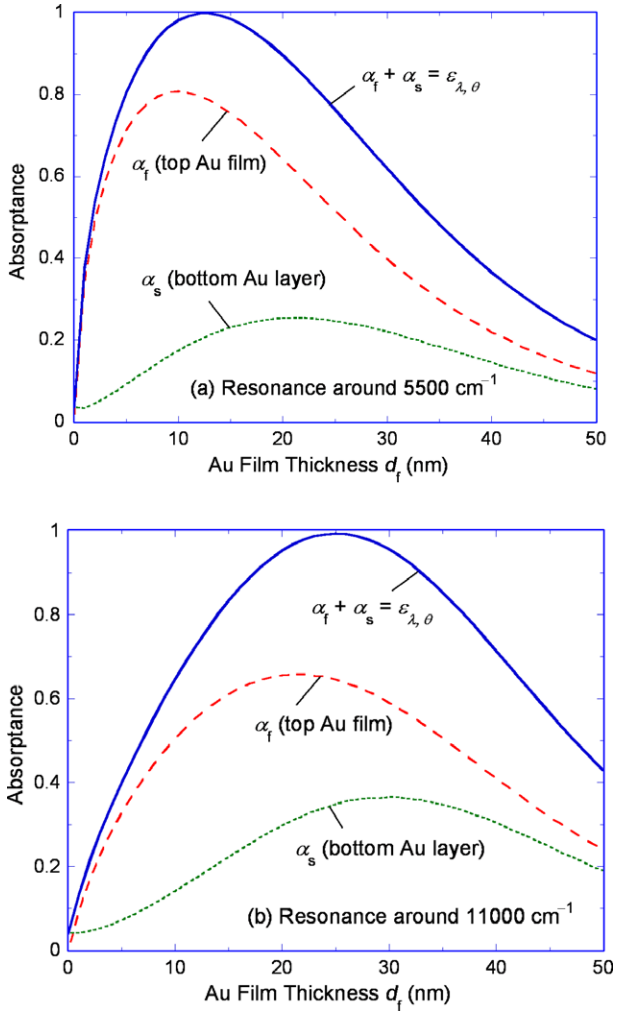

Fig. 4. Absorptances for unpolarized waves at $\theta_i = 10°$, with respect to the top Au film thickness d_f, by the thin Au film and by the opaque Au layer for $d_c = 560$ nm at the resonance wavenumber: (a) around 5500 cm^{-1}; (b) around 11,000 cm^{-1}.

close-to-unity emissivity peak is achieved when $d_f = 25$ nm. In this case, about 60% of the energy is absorbed by the Au film. Because the deposited Au film thickness for the three samples is closer to 25 than 12.5 nm, the first reflectance dip is more sensitive to the Au film thickness than the second dip as seen from Fig. 2.

The spectral reflectance of the Fabry–Perot resonator at other incidence angles is also investigated. Fig. 5 shows the measurements of Sample 1 at 30° and 45° angles of incidence for TE and TM waves, respectively. The model prediction based on the previously obtained thicknesses d_c and d_f for Sample 1 agrees with the experiments well. However, the predicted reflectance minima are much lower than those measured. This may be due to partial coherence of the FTIR spectrometer caused by beam divergence [23]. The resonance frequencies shift toward high frequencies for both polarizations. This is mainly due to the $\cos\theta_c$ terms in the phase shift β. The free spectral range $\Delta\nu$ is tabulated in Table 2 for both the measurement and prediction for each case. The relative difference between the measured and predicted $\Delta\nu$ is within 2.5%, suggesting that the fitting results are pretty reliable. Similar to the resonance frequencies, $\Delta\nu$ also increases with the angle of incidence. It can also be seen that toward large incidence angles, $\Delta\nu$ is larger for TE wave than for TM wave; this is due to the phase shifts associated with the reflection at the cavity boundaries.

Besides temporal coherence demonstrated by the spectral reflectance measurement, the spatial coherence for Sample 1 is shown in Fig. 6 by the angle-resolved reflectance measurement

Table 2
Comparison of the free spectral range $\Delta\nu$ (cm^{-1}) obtained from the spectral reflectance measurement and from the model at $\theta_i = 10°$, 30° (TE and TM waves), and 45° (TE and TM waves) for Sample 1.

	$\theta_i = 10°$	30° TE	30° TM	45° TE	45° TM
Experiment $\Delta\nu$ (cm^{-1})	5050	5306	5246	5692	5546
Model $\Delta\nu$ (cm^{-1})	5142	5422	5376	5798	5688
Relative difference	1.8%	2.1%	2.4%	1.8%	2.5%

at $\lambda = 891$ nm. Reflectance dips are clearly observed at the resonance polar angle: $\theta_0 = 38.4°$ for the TE wave and 43.0° for the TM wave. The polarization-dependent reflection and transmission coefficients at the boundaries are responsible for the variation of resonance angle between the two polarizations. The spectral–directional emissivity, calculated from $\varepsilon_{\lambda,\theta} = 1 - R$ is shown as insets, where the right side is from the measurement and the left side is from model calculation using the same fitting parameters for Sample 1. Contrary to the FTIR measurement at large incidence angles, due to the highly collimated laser beam and the high angular resolution, the reflectance dips or emissivity peaks match very well with those predicted. The relative difference between the measurement and model in terms of the resonance angle is within 2%. It can also be observed that the resonance is much sharper for TE waves than for TM waves. The narrow angular lobes of the spectral–directional emissivity shown in the polar plots clearly demonstrate spatial coherence of the considered Fabry–Perot resonance cavity. The coherence length, defined as $L_{coh} = \lambda/(\pi\Delta\theta\cos\theta_c)$, is used as a measure of the spatial coherence [3,23]. Note that $\Delta\theta$ is the FWHM of the emissivity peak, and the estimated $\Delta\theta$ from the directional measurement is 4.8° and 9.8° for TE and TM waves, respectively.

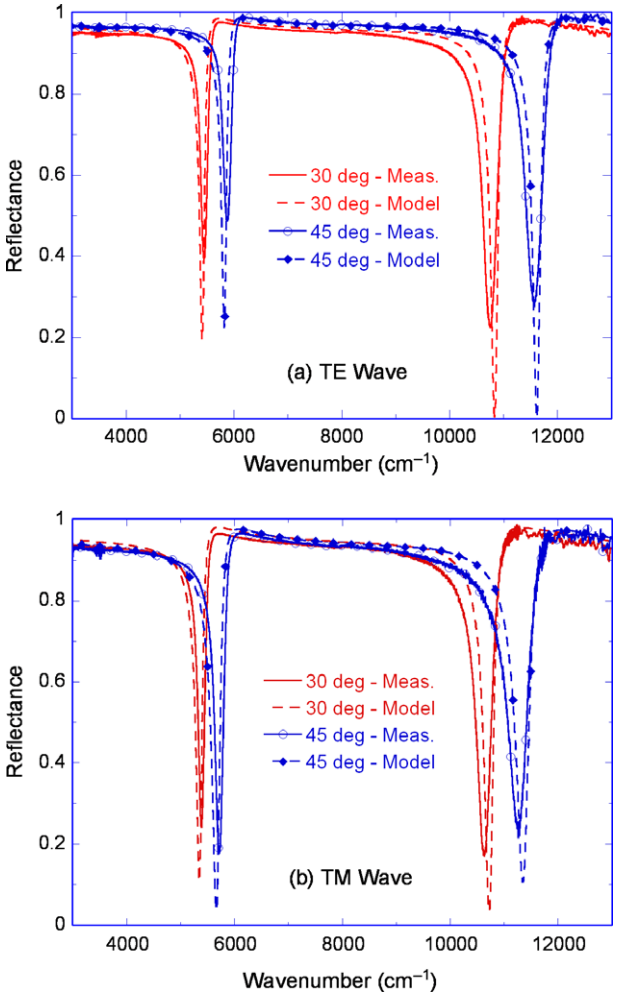

Fig. 5. Spectral reflectance of Sample 1 in the near-IR spectral region at 30° and 45° incidence, respectively: (a) TE wave; (b) TM wave.

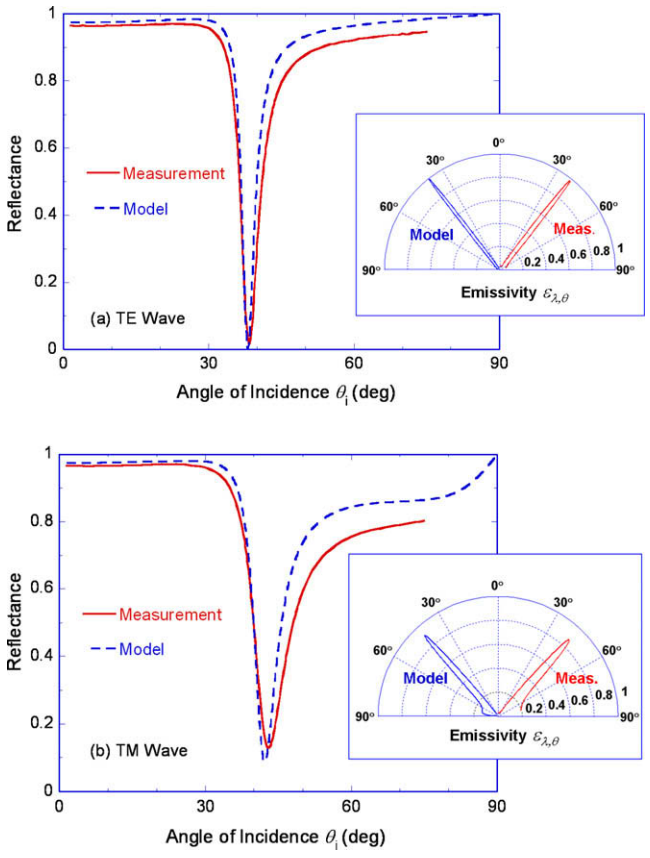

Fig. 6. Spectral reflectance of Sample 1 at $\lambda = 891$ nm: (a) TE wave; (b) TM wave. The insets show the polar plots of the spectral emissivity, $\varepsilon_{\lambda,\theta} = 1 - R$.

The calculated coherence length is 4.85λ and 2.54λ for TE and TM waves, respectively, suggesting that TE waves have better spatial coherence than TM waves for the considered Fabry–Perot resonance cavity structure.

To further investigate the frequency and directional dependence of the emissivity of the proposed structure, the contour plots of the calculated emissivity based on the fitting parameters of Sample 1 are shown in Fig. 7 for TE and TM waves. In Fig. 7, darker colors represent lower emissivity, whereas brighter colors correspond to higher emissivity. The multiple emissivity peaks due to the resonance can be clearly seen as the brightest curves called resonance bands, which exhibit strong spectral and directional selectivity. For comparison, the measurement results of Sample 1 are also plotted as triangles (FTIR) and circles (TAAS), and very good agreement between the measurement and model can be seen.

As the incidence angle increases, the resonance bands are getting narrower for TE waves but wider for TM waves. Besides, there are regions beyond the resonance bands where the emissivity for TM waves is noticeably larger, especially at large incident angles. This is due to polarization-dependent reflectivity at each interface since larger reflectivities at the cavity boundaries would result in sharper resonance peaks [2,17]. To further explain this, the reflectivities, $R_a = r_a r_a^*$ and $R_b = r_b r_b^*$, are plotted in Fig. 8 as functions of the incidence angle θ_i for both polarizations at $\nu = 5000\ \mathrm{cm}^{-1}$ and $\nu = 10{,}000\ \mathrm{cm}^{-1}$, respectively. While the reflectivity $R_s = r_s r_s^*$ between SiO_2 and the bottom Au layer is also important, it does not change very much, since the refraction angle inside SiO_2 is limited to approximately 44° when $\theta_i = 90°$. At the air–Au film and SiO_2–Au film interfaces, there exist large differences in the reflectivity between TE and TM waves at incidence angles greater than 60°. While the reflectance for TE wave increases monotonically with the incidence angle, the reflectance for TM wave is reduced significantly as the incidence angle increases. This is why the resonance bands are much sharper for TE waves than for TM waves. The broader resonance bands of TM waves result from the lower R_b; on the other hand, the reduction of R_a of TM waves at large incidence angles is responsible for the increase in the emissivity outside the resonance bands. It can be seen by comparing Fig. 8a with b that the reflectivity (R_a or R_b) for given polarization and incidence angle is relatively larger at lower frequency, which can explain why the resonance band at the first resonance (lower frequency) is narrower than that at the second resonance (higher frequency) shown in Figs. 2, 5, and 7. Since a thicker Au film will result in higher R_a or R_b, this is why Sample 3 has a smaller $\delta\nu$ than Sample 2.

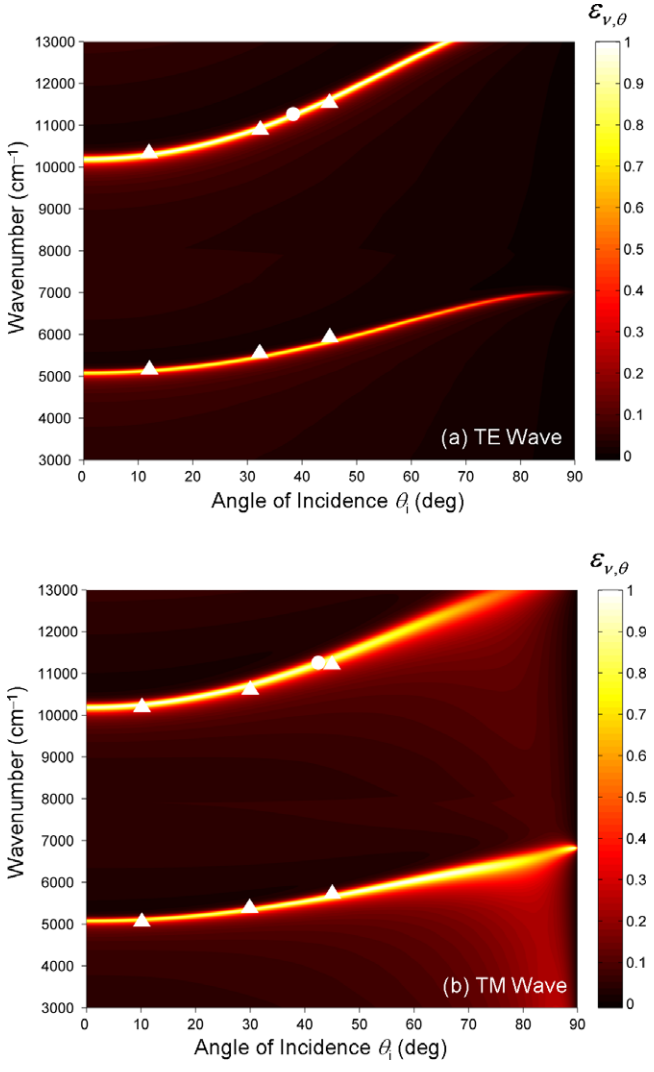

Fig. 7. Contour plots of the spectral–directional emissivity of the considered Fabry–Perot resonator with the fitting parameters of Sample 1: (a) TE wave; (b) TM wave. The triangles represent the reflectance dips measured by the FTIR spectrometer, while the circles indicate the reflectance dips obtained by the laser scatterometer.

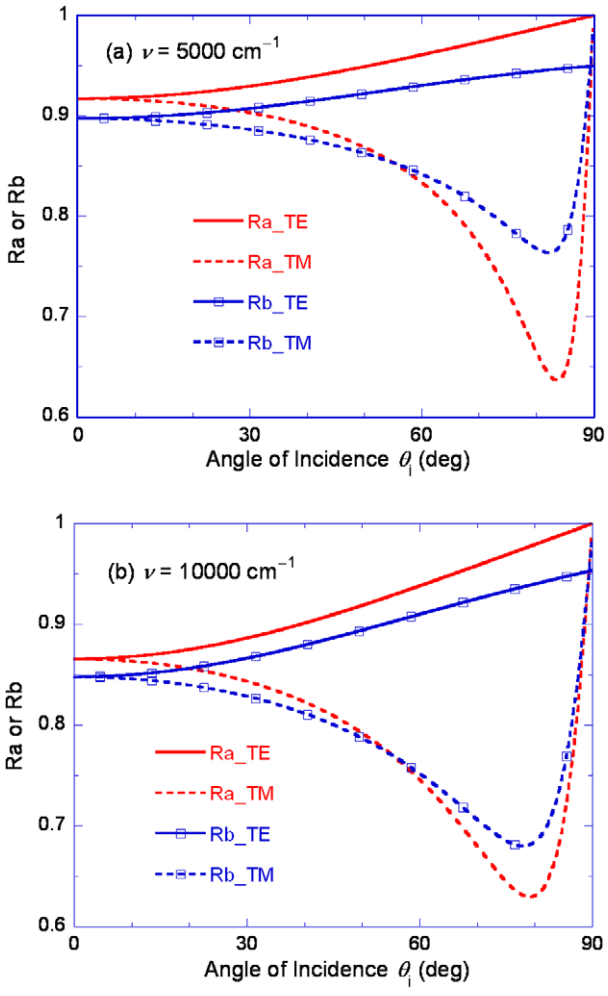

Fig. 8. Calculated reflectance for each polarization at the interface as a function of incidence angle for Au film thickness of 21 nm: (a) at 5000 cm^{-1}; (b) at 10,000 cm^{-1}.

5. Conclusions

This work demonstrates temporal and spatial coherence of thermal radiation of asymmetric Fabry–Perot resonance cavities by measuring the spectral and angle-resolved reflectance using the FTIR spectrometer and a laser scatterometer, respectively. Sharp reflectance dips are observed for both polarizations at several incidence angles. It is found that the resonance frequencies are mainly determined by the cavity thickness but the phase shift due to reflection at the boundaries can modify the resonance frequency to some extend. The top Au film thickness dominantly affects the minimum reflectance or peak emissivity values. Narrow angular lobes of the emissivity are also shown by the angle-resolved reflectance measurement at $\lambda = 891$ nm, which indicates strong directional selectivity and spatial coherence of the sample. The measurement results can be well understood by a detailed theoretical model with fitted film thicknesses. The asymmetric Fabry–Perot resonators have a great advantage in terms of the fabrication as compared with the binary gratings and the truncated photonic crystal structures. The detailed analysis not only enhances the understanding of the coherent emission mechanisms of the asymmetric Fabry–Perot resonators but can also facilitate future design optimization for practical applications in energy conversion systems, such as thermophotovoltaic devices, as well as in thermal management by modifying radiative energy transfer.

Acknowledgements

L.P.W. and Z.M.Z. appreciate the support from the Department of Energy (DE-FG02-06ER46343); X.J.W. and B.J.L. thank the support from the National Science Foundation (CBET-0828701). The samples used in this study were fabricated using facilities at Georgia Tech's Microelectronics Research Center.

References

[1] P.J. Hesketh, B. Gebhart, J.N. Zemel, Measurements of the spectral and directional emission from microgrooved silicon surfaces, J. Heat Transfer 110 (1988) 680–686.
[2] Z.M. Zhang, Nano/Microscale Heat Transfer, McGraw-Hill, New York, 2007 (Chapter 9).
[3] M. Laroche, C. Arnold, E. Marquier, R. Carminati, J.-J. Greffet, S. Collin, N. Bardou, J.L. Pelouard, Highly directional radiation generated by a tungsten thermal source, Opt. Lett. 30 (1988) 2623–2625.
[4] H. Sai, Y. Kanamori, H. Yugami, High-temperature resistive surface grating for spectral control of thermal radiation, Appl. Phys. Lett. 82 (2003) 1685–1687.
[5] B.J. Lee, L.P. Wang, Z.M. Zhang, Coherent thermal emission by excitation of magnetic polaritons between periodic strips and a metallic film, Opt. Express 16 (2008) 11328–11336.
[6] P. Yeh, A. Yariv, A.Y. Cho, Optical surface waves in periodic layered media, Appl. Phys. Lett. 32 (1978) 104–105.
[7] W.M. Robertson, M.S. May, Surface electromagnetic wave excitation on one-dimensional photonic band-gap arrays, Appl. Phys. Lett. 74 (1999) 1800–1802.
[8] J.A. Gaspar-Armenta, F. Villa, Photonic surface-wave excitation: photonic crystal–metal interface, J. Opt. Soc. Am. B 20 (2003) 2349–2354.
[9] B.J. Lee, C.J. Fu, Z.M. Zhang, Coherent thermal emission from one-dimensional photonic crystals, Appl. Phys. Lett. 87 (2005) 071904.
[10] B.J. Lee, Z.M. Zhang, Coherent thermal emission from modified periodic multilayer structures, J. Heat Transfer 129 (2007) 17–26.
[11] B.J. Lee, Z.M. Zhang, Design and fabrication of planar multilayer structures with coherent thermal emission characteristics, J. Appl. Phys. 100 (2006) 063529.
[12] B.J. Lee, Y.-B. Chen, Z.M. Zhang, Surface waves between metallic films and truncated photonic crystals observed with reflectance spectroscopy, Opt. Lett. 33 (2008) 204–206.
[13] E.F. Schubert, N.E.J. Hunt, A.M. Vredenberg, T.D. Harris, J.M. Poate, D.C. Jacobson, Y.H. Wong, G.J. Zydzik, Enhanced photoluminescence by resonant absorption in Er-doped SiO_2/Si microcavities, Appl. Phys. Lett. 63 (1993) 2603–2605.
[14] P. Ben-Abdallah, B. Ni, Single-defect Bragg stacks for high-power narrow-band thermal emission, J. Appl. Phys. 97 (2005) 104910.
[15] I. Celanovic, D. Perreault, J. Kassakian, Resonant-cavity enhanced thermal emission, Phys. Rev. B 72 (2005) 075127.
[16] A.R. Kumar, V.A. Boychev, Z.M. Zhang, D.B. Tanner, Fabry–Perot resonators built with $YBa_2Cu_3O_{7-\delta}$ films on Si substrates, J. Heat Transfer 122 (2000) 785–791.
[17] J.M. Vaughan, The Fabry–Perot Interferometer, Adam Hilger, Philadelphia, PA, 1989.
[18] M. Born, E. Wolf, Principles of Optics, seventh ed., Cambridge University Press, Cambridge, UK, 1999.
[19] Y.-B. Chen, B.J. Lee, Z.M. Zhang, Infrared radiative properties of submicron metallic slit arrays, J. Heat Transfer 130 (2008) 082404.
[20] E.D. Palik, Handbook of Optical Constants of Solids, Academic Press, San Diego, CA, 1998. vols. I and II.
[21] Y.J. Shen, Q.Z. Zhu, Z.M. Zhang, A scatterometer for measuring the bidirectional reflectance and transmittance of semiconductor wafers with rough surfaces, Rev. Sci. Instrum. 74 (2003) 4885–4892.
[22] Q.Z. Zhu, Z.M. Zhang, Correlation of angle-resolved light scattering with the microfacet orientation of rough silicon surfaces, Opt. Eng. 44 (2005) 073601.
[23] B.J. Lee, Z.M. Zhang, Indirect measurements of coherent thermal emission from a truncated photonic crystal structure, J. Thermophys. Heat Transfer 23 (2009) 9–17.